eScience 5 (2025) 100376

Contents lists available at ScienceDirect

eScience

journal homepage: www.keaipublishing.com/en/journals/escience

Research Paper

Elevating Li-ion battery paradigms: Sophisticated ionic architectures in lithium-excess layered oxides for unprecedented electrochemical performance

Jun Ho Yu [a,1], Konstantin Köster [b,c,1], Natalia Voronina [a,1], Sungkyu Kim [a], Hyeon-Ji Shin [d], Kyung Sun Kim [e], Kyuwook Ihm [f], Hyungsub Kim [e], Hun-Gi Jung [d], Koji Yazawa [g], Olivier Guillon [b], Pierluigi Gargiani [h], Laura Simonelli [h,*], Payam Kaghazchi [b,c,*], Seung-Taek Myung [a,*]

[a] Hybrid Materials Research Center, Department of Nanotechnology and Advanced Materials Engineering & Sejong Battery Institute, Sejong University, 98 Gunja-dong, Gwangjin-gu, Seoul, 05006, South Korea
[b] Institute of Energy Materials and Devices - Materials Synthesis and Processing (IMD-2), Forschungszentrum Jülich GmbH, 52425, Jülich, Germany
[c] MESA+ Institute for Nanotechnology, University of Twente, 7500 AE, Enschede, the Netherlands
[d] Center for Energy Storage Research, Korea Institute of Science and Technology, Seoul, 02792, South Korea
[e] Neutron Science Division, Korea Atomic Energy Research Institute (KAERI), 111 Daedeok-daero 989 Beon-Gil, Yuseong-gu, Daejeon, 34057, South Korea
[f] Pohang Accelerator Laboratory, 80 Jigokro-127-beongil, Nam-gu, Pohang, Gyeongbuk, 37673, South Korea
[g] Jeol Resonance Inc, 3-1-1 Musashino, Akishima, Tokyo, 196-8558, Japan
[h] CELLS-ALBA Synchrotron, Cerdanyola del Valles, Barcelona, E-08290, Spain

HIGHLIGHTS

- O2-type layered cathode $Li_{0.75}[Li_{0.15}Ni_{0.15}Mn_{0.7}]O_2$ is a promising cathode for lithium-ion batteries.
- $Li_{0.75}[Li_{0.15}Ni_{0.15}Mn_{0.7}]O_2$ delivers a discharge capacity of 284 mAh g^{-1} and an energy density of 956 Wh kg^{-1}.
- The structural integrity of this O2 structure enables reversible oxygen redox and suppresses phase transition.
- $Li_{0.75}[Li_{0.15}Ni_{0.15}Mn_{0.7}]O_2$|| graphite full cell maintains ~70 % of capacity for 500 cycles at 0.5C.

GRAPHICAL ABSTRACT

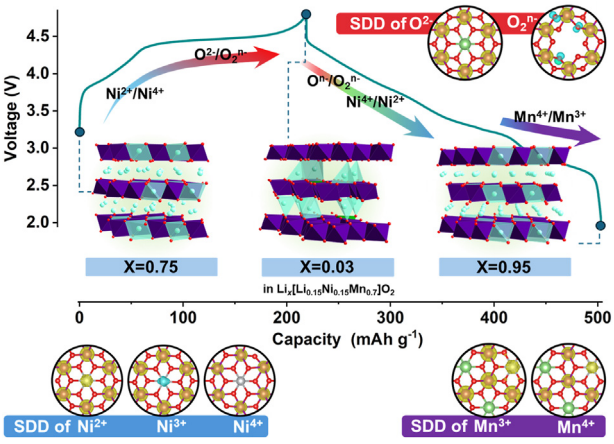

* Corresponding authors.
E-mail addresses: lsimonelli@cells.es (L. Simonelli), p.kaghazchi@fz-juelich.de (P. Kaghazchi), smyung@sejong.ac.kr (S.-T. Myung).
Peer review under the responsibility of Editorial Board of eScience.
[1] These authors contributed equally to this work.

https://doi.org/10.1016/j.esci.2025.100376
Received 5 November 2024; Received in revised form 3 January 2025; Accepted 26 January 2025
Available online 31 January 2025

ARTICLE INFO

Keywords:
Li excess
Layer
Cathode
Lithium
Battery

ABSTRACT

In exploring the frontier of high-energy-density cathode materials for lithium-ion batteries, substantial progress has been made by fine-tuning the composition of Ni-rich cathodes tailored for high-capacity operation. Equally promising are Li-rich cathode materials, which leverage the novel mechanism of oxygen-redox chemistry to achieve enhanced capacities. Nonetheless, the practical realization of these capacities remains elusive, falling short of the desired benchmarks. In this work, we pioneer a Mn-based, Co-free, reduced-nickel, high-capacity cathode material: $Li_{0.75}[Li_{0.15}Ni_{0.15}Mn_{0.7}]O_2$ ionic exchanged from $Na_{0.75}[Li_{0.15}Ni_{0.15}Mn_{0.7}]O_2$. This material is an O2-type layered structure, distinguished by honeycomb ordering within the transition-metal layer, as confirmed by comprehensive neutron and X-ray studies and extensive electrostatic screening. The material's unique structural integrity facilitates the delivery of an exceptional quantity of Li^+ ions *via* $O^{2-}/O_2{}^{n-}$ redox, circumventing oxygen release and phase transition. The de/lithiation process enables the delivery of a substantial reversible capacity of ~284 mAh $(g\text{-oxide})^{-1}$ (956 Wh $(kg\text{-oxide})^{-1}$). Moreover, this structural and chemical stability contributes to an acceptable cycling stability for 500 cycles in full cells, providing improved thermal stability with lower exothermic heat generation and thus highlighting the feasibility of a Mn-based, Co-free, reduced-nickel composition. This investigation marks a pivotal advancement in layered lithium cathode materials.

1. Introduction

Layered structured materials have demonstrated significant success as cathode materials for commercial lithium-ion batteries (LIBs) due to their facile movement of Li^+ ions, substantial reversible capacity, and acceptable cyclability [1–3]. However, advances in LIB performance have become imperative due not only to ever-growing demands in the portable and stationary markets but also to the recent escalation of geological and environmental concerns. Thus, new cathode materials are needed to enhance the energy density of LIBs. Lithium cobalt oxide [4] and lithium nickel oxide [5,6] have set benchmarks as cathode materials, offering high capacity, excellent cyclability, and facile lithium-ion mobility. Spinel $LiMn_2O_4$ stands out for its superior thermal stability and rate capability [7], while transition metal-substituted variants like $LiNi_{0.5}Mn_{1.5}O_4$ achieve a high voltage plateau of ~4.7 V [8]. These merits converge in the Mn-based Li-rich material Li_2MnO_3 [9,10], which integrates high capacity through lattice oxygen redox reactions, facilitating lithium migration at transition-metal sites and band reshuffling to enhance electrochemical performance. Unfortunately, poor activation and a dependency on anionic redox for charge compensation detract from its appeal as a practical cathode material. A novel approach involving the introduction of Ni into Li-rich Li_2MnO_3 results in the formation of $Li_{1.0}[Li_{0.2}Ni_{0.2}Mn_{0.6}]O_2$, which exhibits significantly enhanced electrochemical performance, characterized by exceptionally high energy density and improved kinetics that are driven by the synergistic contributions of Ni and O in the redox reactions [11,12]. Nevertheless, challenges such as ongoing oxygen loss and irreversible phase transition to the spinel phase must be resolved.

Li-excess O2-type layered crystal frameworks have been investigated as potential cathode materials due to their unique structural and electrochemical properties. These materials are defined by their ABCB oxygen stacking arrangement, which differs from the ABCABC stacking observed in O3-type layered structures. The O2-type framework features wide interlayer *d*-spacing while maintaining a compact *a*-axis parameter [13–15]. This structural configuration facilitates Li^+ diffusion, thereby enhancing rate capability. Among these materials, Li-excess structures such as $Li_x[Li_yNi_zMn_{1-y-z}]O_2$ (typically, $x \leq 1$) are particularly noteworthy for their ability to provide stable cycling without the significant phase transitions known to degrade the electrode performance in conventional O3-type Li-rich cathodes [11,16–21]. Furthermore, the O2-type Li-excess layered compounds are activated by dual redox pairs such as transition metals (TM) and lattice oxygen, which simultaneously induce high capacity and energy density [22–26]. Introducing cobalt (Co) and nickel (Ni) in O2-type lithium layered oxides has been shown to enhance structural stability during cycling, suppress voltage hysteresis during charge and discharge, and improve electrical conductivity [1,3,13–15, 22–34]. Specifically, the incorporation of Ni element contributes to higher operating voltages, while the enhanced conductivity provided by Co promotes both initial Coulombic efficiency and rate capability. It is, however, interesting to note that recent studies have indicated the trade-offs and complexities associated with these dopants in O2-type cathode materials. For instance, Kang et al. [30] compared Co^{3+} and Ni^{2+} substitutions, demonstrating that aliovalent Co^{3+} has a greater tendency than Ni^{2+} to disrupt the cation ordering of the honeycomb superstructure in the TM layer. This disintegration may result in TM migration within the structure during cycling, causing structural degradation that gradually deactivates the oxygen redox reaction, which plays a key role in achieving high capacity in O2-type lithium layered oxides. Yamada et al. [34] successfully substituted Co in O2–$Li_{1.25-y}Mn_{0.5}Co_{0.25}O_2$ with Ni, producing Co-free O2–$Li_{1.12-y}Mn_{0.71}Ni_{0.17}O_2$. Although the Co-free composition exhibited a slightly lower initial Coulombic efficiency, it demonstrated better electrode performance in terms of cyclability. Xia et al. [27] investigated $Li_{1.25}Co_{0.25}Mn_{0.50}O_2$ stabilized into an O2-type layer structure and reported an extraordinary reversible capacity of 400 mAh g^{-1}. However, while this value exceeds the theoretical capacity, the resulting cycling stability did not ensure the material's feasibility for long-term use. Wang et al. [32] proposed a combined strategy involving a $Li_{1.2}Ni_{0.13}Co_{0.13}Mn_{0.54}O_2$ cathode paired with a fluorinated electrolyte. Their work presented remarkable performance, including an initial Coulombic efficiency of 99.82%, excellent cycling stability, and a reversible capacity of 278 mAh g^{-1}. These findings emphasize the importance of compositional engineering with Ni to harness its stabilizing effects in Co-free O2-type Li-excess cathode materials, presenting viable pathways for achieving high performance and structural stability while minimizing the dependence on Co.

Herein, we synthesized O2-type Li-excess $Li_{0.75}[Li_{0.15}Ni_{0.15}Mn_{0.7}]O_2$ (LLNM) through ion exchange from P2-type $Na_{0.75}[Li_{0.15}Ni_{0.15}Mn_{0.7}]O_2$. The theoretical capacity of O2-LLNM was determined to be 313 mAh g^{-1}, providing clarity on ambiguities found in previous research on O2-type materials. To gain a deeper understanding of its structural evolution and chemical states during electrochemical reactions, we refined and thoroughly analyzed the structure using a range of advanced analytical techniques. These investigations revealed the dynamics of the material's charge-transfer mechanisms, which involved lithium migration across both the Li layer and the TM sites, including coordination or chemical-state transitions of TMs and oxygen. The LLNM delivered an exceptionally high capacity of 284 mAh g^{-1} (956 Wh kg^{-1}), propelled by the Li-excess structure maximizing the participation of lithium in the reaction; this was maintained through the redox activities of both cations and anions during extensive cycling, effectively mitigating phase transitions and minimizing oxygen loss during the oxygen redox reactions.

2. Results and discussion

As-synthesized P2–$Na_{0.75}[Li_{0.15}Ni_{0.15}Mn_{0.7}]O_2$ (NLNM) was ion-exchanged with LiOH at 280 °C for 1 h in air. The NLNM was crystallized into a layered structure with the *P6₃* space group (Fig. S1 and Table S1). X-ray absorption near edge spectroscopy (XANES) analysis verified that the average oxidation states of Ni and Mn were 2+ and 4+, respectively (Fig. S2). The Bragg peaks observed at 20.6° and 22.1° (2θ) indicated the emergence of Li/Ni ordering forming a $\sqrt{3}a \times \sqrt{3}a$ type supercell in the TM layer (Fig. S1 inset), which resulted from the difference between the ionic radii of Li^+ (0.76 Å) and Ni^{2+} (0.69 Å) and that of Mn^{4+} (0.53 Å). Ion exchange with LiOH did not result in unreacted Na content, as indicated by the energy-dispersive X-ray spectroscopy (EDS) mapping image and the inductively coupled plasma atomic emission spectroscopy (ICP-AES) data (Fig. S3 and Table S2). The ion-exchanged result was analyzed by Rietveld refinement of the X-ray diffraction (XRD) and neutron powder diffraction (NPD) patterns (Fig. 1a, Fig. S4–S5, and Tables S3–S4); the NPD data indicated an O2-type hexagonal structure as the major phase (97.4%) and two minor phases, Li_2MnO_3 (1.42%) and cubic spinel $Li[Ni_{0.5}Mn_{1.5}]O_4$ (1.18%). The corresponding interlayer distance was reduced to 4.83 Å from 5.51 Å after the ion exchange. The XANES results for the Ni K-edge showed no change in the oxidation state of Ni before and after the ion exchange (Fig. 1b). In addition, the resulting oxidation state of Mn was almost identical to before the ion exchange, tetravalent Mn (Fig. 1c). Selected-area electron diffraction (SAED) along the [1 $\bar{1}$ 0] direction of LLNM indicated an ordered layered structure with a uniform interlayer distance of ~4.84 Å (Fig. 1d). In addition, high-angle annular dark-field scanning transmission electron microscopy (HAADF-STEM) revealed the presence of dumbbell-like spots, which represent Li–TM–TM–Li elements aligned along the [110] direction (Figs. 1e and f). Namely, the one-third absent signal reflects the unique regularity of honeycomb ordering such as Li-TM-TM-Li in the [110] zone axis (Li is not visible due to the low electron density of Li element), corresponding to the *a-b* plane, which is in agreement with earlier reports on O2-type layered compounds [23,25,27,35,36]. The ionic exchange process is topotactic, resulting in the planar and localized translation of TM layers in various directions, creating octahedral sites where lithium ions are more stabilized. TM layers can glide along multiple directions, simultaneously acting at many different points within the particles while causing imperfections and stacking faults. The complexity of this process arises from the non-uniform gliding of layers during the transition from the Na-based P2-type to the Li-based O2-type phase. The consequent presence of O2/O4/O6 intergrowth (stacking fault) observed in the STEM images (Figs. 1e, f, and S6) further verifies the complexity of the process and the random gliding typically observed in O2-type layer structures [28]. In addition, the STEM image reveals the O2-type stacking sequence, interspersed with intergrowths of O4 and O6 symmetry. The O2 structure is characterized by low symmetry, which is influenced by the random nature of the ion-exchange process. The random gliding induces rotational stacking faults, leading to the formation of O4 stacking with higher symmetry. A further increase in the symmetry results in a rhombohedral structure with O6 stacking [3,14,37–39]. Moreover, during ion exchange, the spinel phase is formed on the surface of the O2-layered phase while preserving the overall O2 crystal orientation. This occurs at a slightly elevated temperature of 280 °C, where the spinel phase, identified to be $Li[Ni_{0.5}Mn_{1.5}]O_4$, becomes thermodynamically more stable than the O2-layered phase [2,8]. It is likely that the $Li[Ni_{0.5}Mn_{1.5}]O_4$ spinel domain, observed at the surface in Fig. 1e, partially promotes the surface stability of the O2 phase due to its robust structure at high voltage.

NPD confirmed that the Li, Ni, and Mn elements are situated at the specified coordinates within the TM layer based on the $P6_3mc$ space group. However, according to the literature, no space group has yet been identified to distinguish the Li and Ni elements from the Mn elements in the TM layer. The honeycomb-like ordering of LLNM is attributed to the similar ionic radii of Li^+ and Ni^{2+}, leading to them sharing the same sites relative to Mn^{4+} and their occupancy constituting one-third of the TM site. If Li alone were responsible for the ordering, the smaller occupancy would result in ribbon ordering [35]. The distinct neutron scattering lengths (Li-6: 2.00 fm, Li-7: 2.22 fm, Ni: 10.3 fm, Mn: 3.73 fm) enable the differentiation of Li, Ni, and Mn elements using the *P1* space group (Fig. S7 and Table S5) [40], which is available to distinguish the superlattice ordering of $LiMn_6$ and $NiMn_6$ coordination. We employed density functional theory (DFT) geometry optimizations and machine-learning force-field (MLFF) *ab initio* molecular dynamics (AIMD) simulations. Thus, we were able to study the lattice parameter changes at different states of charge. Fig. S8 shows the evolution of the energy, temperature, and pressure over the simulation time for all the MD runs. In addition, honeycomb ordering is electrostatically strongly favored in $Li_{0.75}[Li_{1/6}Ni_{1/6}Mn_{2/3}]O_2$ (Li^+, $Ni^{2.5+}$, Mn^{4+}, O^{2-}), as the Coulombic energy of the lowest energy configuration with a non-perfect honeycomb ordering in one of the two TM layers is ~4.7 eV higher (Fig. 1g). Even though electrostatic energy is a fairly rough approximation, the obtained energy difference is quite severe, and there are plenty of lower-energy configurations with honeycomb ordering in both TM layers but different shifts of the TM layers towards each other and/or different Li arrangements in the Li layer, indicating that a honeycomb ordering in $Li_{0.75}[Li_{1/6}Ni_{1/6}Mn_{2/3}]O_2$ is also electrostatically strongly favored.

3. Electrochemical test

The fabricated LNNM electrode (theoretical capacity: 308 mAh g^{-1}, assuming 1 mol Li insertion per formula unit) was tested in the voltage range of 2–4.8 V with a constant current of 30 mA g^{-1} (0.1C) at 25 °C. A gradual rise in the operation voltage to 4.35 V was observed, with the delivery of a charge capacity of ~67 mAh g^{-1}, corresponding to the extraction of 0.22 mol of Li per formula unit (Fig. 2a). In this range, the only possible reaction by TMs is the oxidation of Ni^{2+} toward Ni^{4+}, because in this range, Mn^{4+} is inactive in an octahedral environment. Further delithiation resulted in the emergence of a long voltage plateau above 4.35 V. The delivered capacity was 155 mAh g^{-1}, corresponding to the extraction of 0.50 mol of Li per formula unit. As there were no active species to participate in the electrochemical activity, oxidation of the lattice oxygen was the only possible trigger of the charge compensation with Li^+ ions. The total charge capacity was thus ~222 mAh g^{-1} on charge, compensated for by the extraction of 0.72 mol Li from the host structure. On discharge, no large voltage plateau above 4.35 V was observed, and the voltage gradually decayed to 3.4 V with a capacity of 132 mAh g^{-1} (0.43 mol Li per formula unit). Further lithiation to 2.97 V was compensated by delivering a capacity of 78 mAh g^{-1} (0.25 Li per formula unit), below which an addition plateau was perceived to 2 V by delivering a capacity of 74 mAh g^{-1} (0.24 Li per formula unit). Note that a large discharge capacity, ~284 mAh $(g\text{-oxide})^{-1}$ (956 Wh kg^{-1}), corresponding to 0.92 mol Li per formula unit, was available in the tested range. The reversible reaction was observed for the second charge and discharge. Although there was a hysteresis for the first cycle, the consecutive de/lithiation mitigated the large difference in operation for further cycles (Fig. 2a and Fig. S9). The O2-LLNM electrode maintained its initial capacity to ~75% (213 mAh g^{-1}) at 0.1C for 200 cycles (Fig. 2b). At 1 and 2C, the observed capacities were 208 and 191 mAh g^{-1}, respectively. Further testing at 0.5C also demonstrated the compatibility of O2-LLNM, with a retention of ~92.5% (226–209 mAh g^{-1}) for 100 cycles (Fig. 2c), in addition to an activity at 6C of 104 mAh g^{-1}. Long-term electrode stability was confirmed by using full cells comprised of a graphite anode and an O2–$Li_{0.75}[Li_{0.15}Ni_{0.15}Mn_{0.7}]O_2$ cathode, tested in the voltage range of 2.1–4.7 V (Figs. 2d–f). Pre-cycles were performed for the cathode to supply it with deficient lithium, adjusting the anode and cathode capacity ratio to 1.2. The full cell delivered an initial discharge capacity of 272 mAh g^{-1} at 0.1C (Fig. 2d).

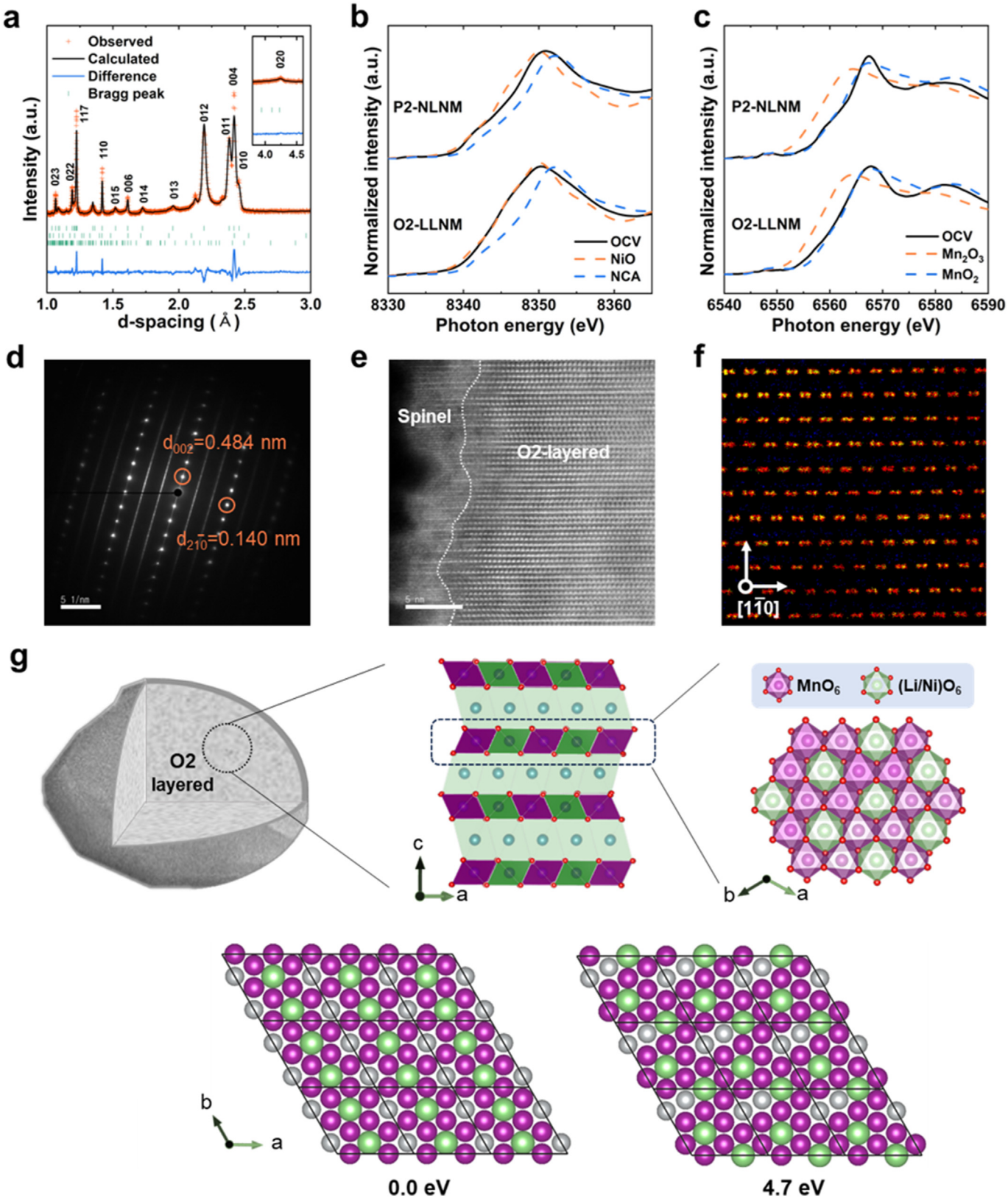

Fig. 1. Material characterization. (a) Rietveld refinement result for NPD pattern of LLNM. (b) XANES spectrum of NLNM and LLNM for Ni K-edge. (c) XANES spectra of NLNM and LLNM for Mn K-edge. (d) SAED pattern for LLNM. (e, f) STEM image and magnified image of LLNM along [1 $\bar{1}$ 0] zone axis. (g) Schematic illustration of (top) honeycomb ordering in the a-b plane and (bottom) difference in electrostatic energy for most favorable ionic configuration (left, normalized to 0 eV) and (right) lowest energy configuration with a non-perfect honeycomb ordering in one of the TM layers of O2–$Li_{0.75}[Li_{1/6}Ni_{1/6}Mn_{2/3}]O_2$ (Li^+, $Ni^{2.5+}$, Mn^{4+}, O^{2-}).

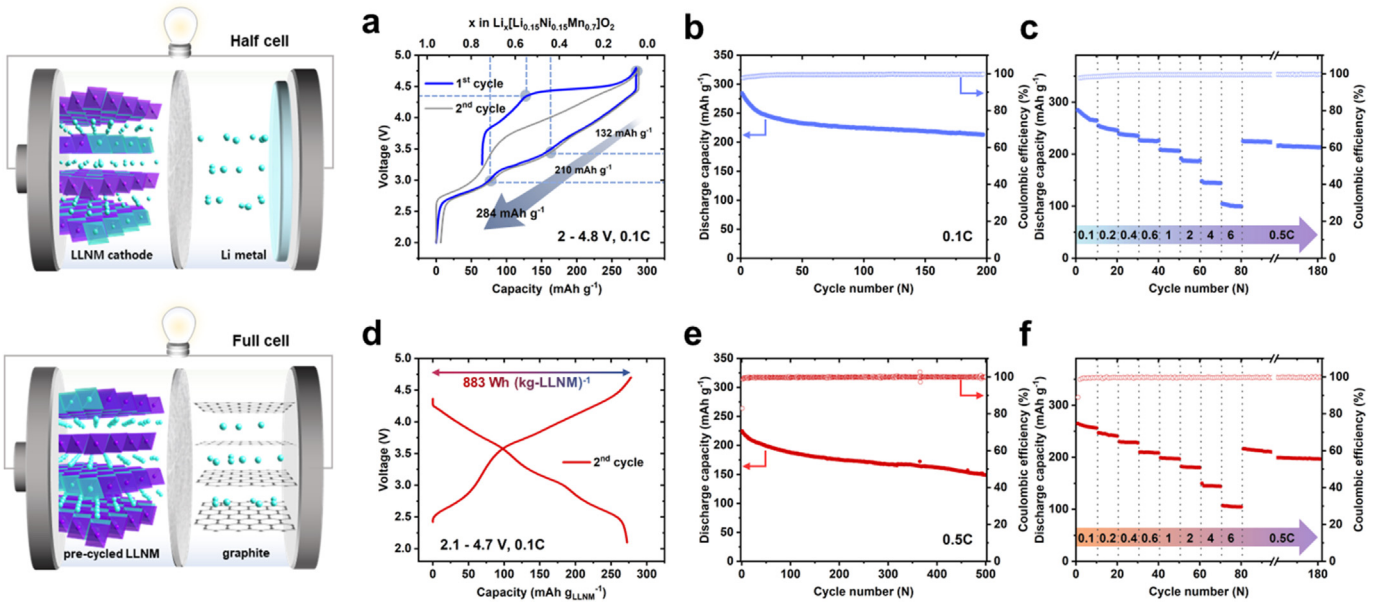

Fig. 2. Evaluation of electrochemical performance. (a) Voltage profile of LLNM under constant current of 30 mA g^{-1}. (b) Cycling performance of LLNM over 200 cycles. (c) Rate capability of LLNM at various C-rates. (d) Voltage profile of LLNM||graphite full cell under constant current of 30 mA g^{-1}. (e) Cycling performance of LLNM||graphite full cell over 200 cycles. (f) Rate capability of LLNM||graphite full cell at various C-rates.

The slight change in the voltage profile resulted from the use of a graphite anode. The capacity gradually decayed upon cycling, with a retention of ~70% after 500 cycles at 0.5C (Fig. 2e and Fig. S10). The rate capability presented a similar tendency as that for the half cells (Fig. 2f). From the above viewpoint, the Mn-based, Co-free, reduced-nickel O2–$Li_{0.75}[Li_{0.15}Ni_{0.15}Mn_{0.7}]O_2$ cathode presents promising electrode performance.

The LLNM electrode was investigated using *operando* XRD (*o*-XRD). The *o*-XRD patterns displayed reversible peak shifts for the two cycles (Fig. 3a). The peaks belonging to the O2 phase at 18.5°, 37.2°, and 46.5° (2θ), corresponding to the (002), (004), and (013) planes, shifted, and the resulting *a*- and *c*-axis parameters decreased as the ionic radii of Ni decreased (Ni^{2+}: 0.69 Å, Ni^{3+}: 0.56 Å, and Ni^{4+}: 0.48 Å) (Fig. 3b). For $x \leq 0.53$ in $Li_x[Li_{0.15}Ni_{0.15}Mn_{0.7}]O_2$, which represents a long voltage plateau over 4.35 V, the movements of the (002) and (004) peaks further progressed by the end of delithiation to $x = 0.03$ in $Li_x[Li_{0.15}Ni_{0.15}Mn_{0.7}]O_2$ (Fig. 3a), reflecting gradual decreases in the *a*- and *c*-axis parameters in Fig. 3b. Indeed, a change in the *a*-axis parameter is usually induced by the oxidation of TM elements. Lithiation induced the recovery of the Bragg peak intensity and positions (Fig. 3a). In addition, no new phases

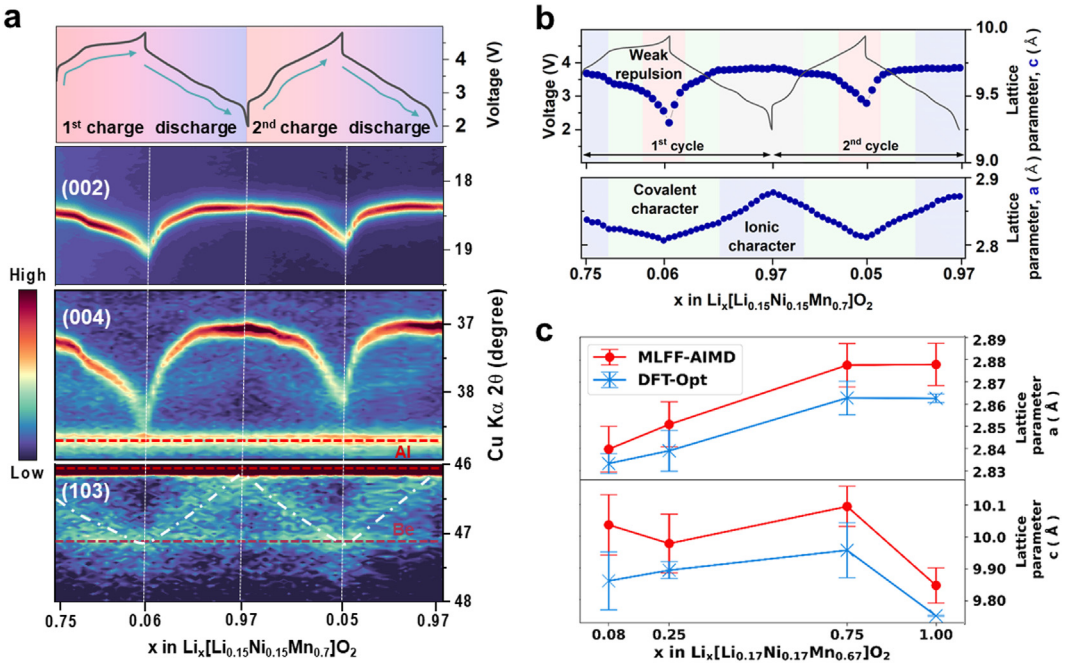

Fig. 3. Structural evolution during charge and discharge. (a) Contour plot of *o*-XRD result for LLNM electrode during 2 cycles. (b) Voltage profile of LLNM and corresponding parameters a and c. (c) Calculated lattice parameters at different charge states as obtained from MLFF-AIMD runs, as well as DFT optimization of different MD images, including their standard deviations as error bars.

were formed during discharge (reduction). The resulting *a*- and *c*-axis parameters both increased upon discharge (Fig. 3b). This rise of the *c*-axis parameter is related to the weakening of the covalent character in the interslab. The variation of the *c*-axis became less steep from $x \approx 0.46$ in $Li_x[Li_{0.15}Ni_{0.15}Mn_{0.7}]O_2$, although the *a*-axis value increased progressively until the end of discharge. The lattice parameters of MLFF-AIMD simulations are always larger than those obtained from DFT optimizations, which can be attributed to thermal expansion of the cathode material, as MLFF-AIMD simulations are conducted at room temperature whereas DFT optimizations are, by definition, at 0 K. The resulting evolution of the *a*- and *c*-lattice parameters is shown in Fig. 3c. In agreement with the experimental XRD data in Figs. 3a and b, the *a*-lattice parameter decreased almost linearly on charge, even though the simulations showed no significant increase between $x = 1.00$ and $x = 0.75$ in $Li_x[Li_{0.15}Ni_{0.15}Mn_{0.7}]O_2$. This behavior might be explained by the simulated lithium concentration of exactly one not being reached in the experiment. The overall trend of the *a*-lattice parameter might be explained by the change of the ionic radii in the TM layer on charge/discharge, as discussed in the experimental results section. On charge, a decrease of the *c*-lattice parameter from $x = 0.75$ to $x = 0.08$ was also observed for the calculated structures, as shown in Fig. 3c, with an outlier in the MLFF-AIMD data for $x = 0.08$. That is, however, still within the error estimated by the standard deviation over simulation time. A disagreement with the experimental results was observed at $x = 1.00$, which can be again attributed to the higher lithium concentration in the simulation compared to the experiment. The low error bars (for the *a*-lattice parameter as well) suggest that the fully lithiated structure is perfectly ordered and therefore relatively "stiff" in the MLFF-AIMD simulations, likely making the structural model not directly comparable to the less-than-perfect experimental one.

The redox reactions were confirmed through *o*-XANES spectra to $x \approx 0.53$ in $Li_x[Li_{0.15}Ni_{0.15}Mn_{0.7}]O_2$, which belongs to the end of the ascending voltage profile; the Ni^{2+} was gradually oxidized toward Ni^{4+} (Fig. 4a). The Mn, which was tetravalent, was not active during charge (Fig. 4b). Note that the observed capacity was too high in the oxidation of 0.15 mol of Ni^{2+} toward Ni^{4+}; therefore, it is reasonable to consider additional oxidation processes induced by the lattice oxygen of $Li_x[Li_{0.15}Ni_{0.15}Mn_{0.7}]O_2$. The oxygen K-edge spectra clearly present a t_{2g} and e_g hybridized orbital of Mn 4*d* – O 2*p*, appearing at 528.5 and 531 eV (Fig. 4c). The emergence of the shoulder peak at 530 eV is attributed to overlapping of the t_{2g} and e_g orbitals of O 2*p*. This result likely indicates the formation of dimerized lattice oxygen, O_2^{n-} ($n < 2$). The electrostatic repulsion force of the facing O–O can be weakened by the oxidation of lattice oxygen. In addition, a covalent character affecting the structure by the formation of Ni^{4+} in turn induces a decrease in the interlayer distance along the *c*-axis.

The oxidized Ni^{4+} was reduced to Ni^{2+} in the range of $x \leq 0.71$ in $Li_x[Li_{0.15}Ni_{0.15}Mn_{0.7}]O_2$, according to the Ni K-edge *o*-XANES spectra (Fig. 4a). In addition, the tetravalent Mn was reduced toward Mn^{3+} in the range of $x \geq 0.71$ in $Li_x[Li_{0.15}Ni_{0.105}Mn_{0.7}]O_2$, as the photon energy shift was evident toward lower values (Fig. 4b). After discharge, the O K-edge spectrum was identical to that of the fresh state (Fig. 4c). The increase in the *a*-axis induced more ionic character in the interslab, such that repulsion between the interlayer was somewhat diminished, emerging in the range of $x \geq 0.46$ in $Li_x[Li_{0.15}Ni_{0.15}Mn_{0.7}]O_2$ as a result of more Li^+ insertion into the structure occurring toward the end of discharge. The same tendency was observed during the second cycle. Although large charge and discharge capacities were delivered during the de/lithiation process, the original O2 phase did not undergo observable phase separation or phase transition.

As also suggested by the experimental results, the oxygen distances in the MLFF-AIMD simulations decrease by charging the cathode material according to the computed pair-distribution functions (PDFs) in Fig. 4d. Peak shifts at larger distances in the PDFs towards lower distances with lower *x*, e.g., the peak directly below 4 Å, can probably be attributed mainly to the aforementioned changes in lattice parameters. The peaks in the PDFs are also slightly broader and significantly less intense on charge because the whole structure becomes slightly more disordered, as

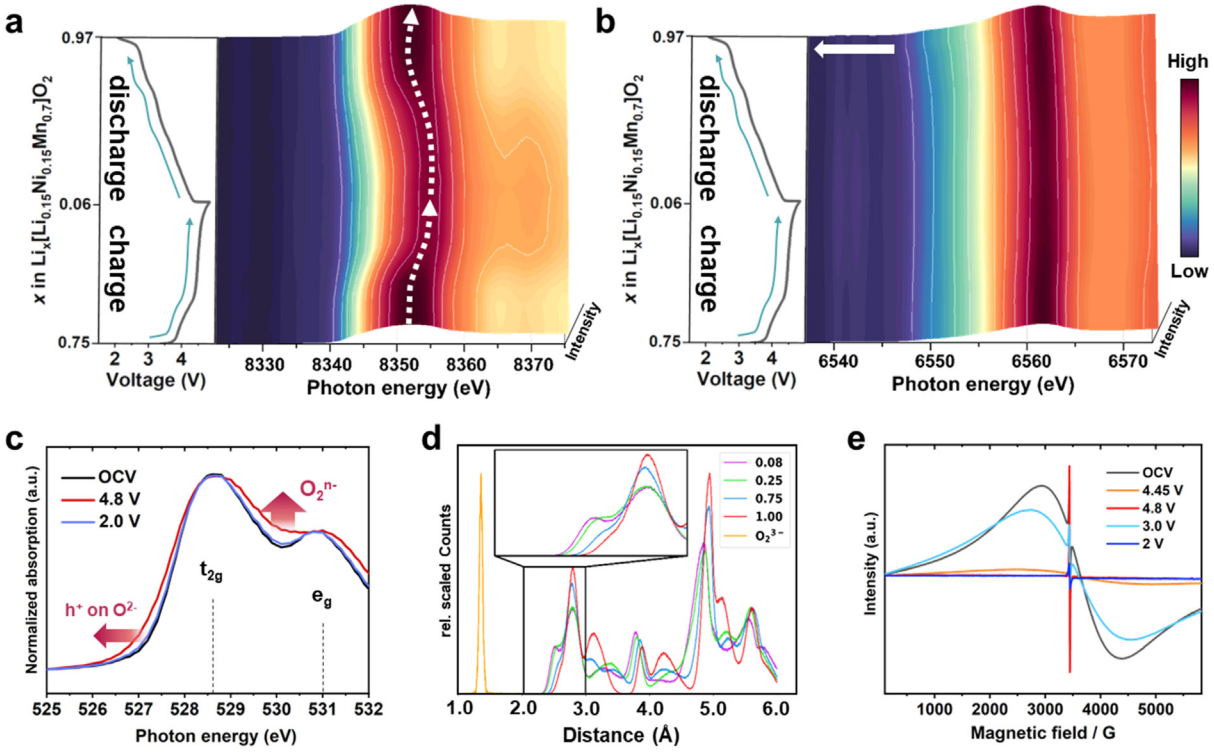

Fig. 4. Redox compensation mechanism. (a) *Operando* XANES result of LLNM for Ni K-edge. (b) *Operando* XANES result of LLNM for Mn K-edge. (c) XANES result of LLNM for O K-edge. (d) Scaled O–O PDFs averaged over time through the MLFF-AIMD runs, along with PDF from an MLFF-AIMD simulation of an O_2^{3-} dimer. (e) EPR result for LLNM electrode material at different states of charge and discharge.

previously discussed. At the nearest-neighbor distance peak at ~2.8 Å, a shoulder starts to emerge at lower distances for $x = 0.25$, becoming even more profound at $x = 0.08$. Since oxygen redox is expected to occur at these lithium concentrations, as observed both experimentally and theoretically, this peak might indicate the start of lattice oxygen dimerization, as seen in the XANES spectra for experimental oxygen in Fig. 4c. However, the peak shifts are small, and the appearance of a dimer (partial or fully covalent bond) is unlikely. These findings give rise to the conclusion that even though strong oxygen redox is active in the LNNM cathode, no oxygen dimers form, which prevents the irreversible loss of oxygen during cycling. This conclusion is also in accordance with the experimental DEMS measurements in Fig. S11.

As mentioned in relation to Fig. 4c, we confirmed that the oxidation behavior of the lattice oxygen was reversible on discharge, since the fresh spectrum was almost identical to the discharged one. To investigate the nature of the lattice oxygen on charge, we analyzed the electronic state of Mn and O present in the *ex situ* electron paramagnetic resonance (EPR) spectra measured under the perpendicular polarization mode at 50 K (Fig. 4e). The fresh LLNM powder exhibited a broad Lorentzian resonance signal, indicative of antiferromagnetic coupling between Mn^{4+} in configuration ($t_{2g}{}^3e_g{}^0$) and O^{2-}, with a *g*-value of ≈ 1.99. The broadening of the EPR signal in LLNM is attributed to the presence of Ni^{2+} in the material, which promotes ferromagnetic interactions between Ni^{2+} ($t_{2g}{}^6e_g{}^2$) and Mn^{4+} ($t_{2g}{}^3e_g{}^0$) ions [41–43]. Furthermore, the presence of a carbon conducting agent typically induces a sharp signal corresponding to free electrons from carbon, with a *g*-value of ≈2.00 [44]. Upon the electrode being charged to 4.45 V ($x = 0.43$ in $Li_x[Li_{0.15}Ni_{0.15}Mn_{0.7}]O_2$), the resonance signal flattened because the antiferromagnetic interactions between Ni^{4+}-*O*-Mn^{4+} were stronger than those between Ni^{2+}-*O*-Mn^{4+}. The signal became further flattened after charging to 4.8 V ($x = 0.03$ in $Li_x[Li_{0.15}Ni_{0.15}Mn_{0.7}]O_2$). According to the *o*-XANES analysis (Figs. 4a and b), the average oxidation states of Ni and Mn were confirmed to be tetravalent in the plateau region. Therefore, significant changes in the resonance signal were not expected during delithiation within this region. Nevertheless, as Mn remained tetravalent in the ($t_{2g}{}^3\,e_g{}^0$) configuration during charging, the observed decline in the resonance signal suggests that lattice oxygen was oxidized to $O_2{}^{n-}$ ($n < 2$), leading to diminished super-exchange interactions. This finding aligns with the O K-edge XANES data (Fig. 4c). Upon discharging to 3.0 V ($x = 0.71$ in $Li_x[Li_{0.15}Ni_{0.15}Mn_{0.7}]O_2$), the resonance signal recovered due to the reversible reduction of Ni^{4+} to Ni^{2+} and the stabilization of Mn^{4+} ($t_{2g}{}^3e_g{}^0$) with O^{2-}. After lithiation to 2.0 V ($x = 0.95$ in $Li_x[Li_{0.15}Ni_{0.15}Mn_{0.7}]O_2$), where the oxidation state of Mn fell below 4+ (≈3.7+), the Lorentzian resonance signal flattened again. This is attributed to the presence of $Mn^{3+}(t_{2g}{}^3e_g{}^1)$ – O^{2-} within the TM layer.

The resulting Li^+ diffusion, D_{Li^+}, was also dependent on each redox pair (Fig. S11a). In the early stages of charging, relatively fast diffusivity to ~10^{-9} $cm^2\,s^{-1}$ was observed along with the Ni^{2+}/Ni^{4+} redox. From x ≈ 0.53 in $Li_x[Li_{0.15}Ni_{0.15}Mn_{0.7}]O_2$, the resulting diffusion progressed rather slowly, decreasing to ~10^{-13} $cm^2\,s^{-1}$ and with notable fluctuation to the end of charge. From the above findings, it is apparent that the oxidation of the lattice oxygen is responsible for the slow charge compensation. The slow kinetics continued to the initial discharging, which belongs to the reduction of oxygen. Then, the diffusion increased to ~10^{-11} $cm^2\,s^{-1}$ due to the reduction of Ni^{4+} to Ni^{2+}. Further lithiation induced the rise of diffusion to the end of discharge, compensated for by Mn^{4+}/Mn^{3+} redox. It is worth noting that O_2 and CO_2 evolution were not visible during the first cycle (Fig. S11b). This finding demonstrates that the associated oxygen redox did not induce molecular O_2 evolution but contributed to the charge compensation during charge and discharge.

Using the optimized lowest energy structures, we employed DFT-HSE06 to calculate the electronic structures in order to study the underlying redox mechanism from a theoretical perspective. The spin-polarized calculations allow the spin density difference (SDD) to be obtained, from which the number of unpaired electrons (UPEs) per ion

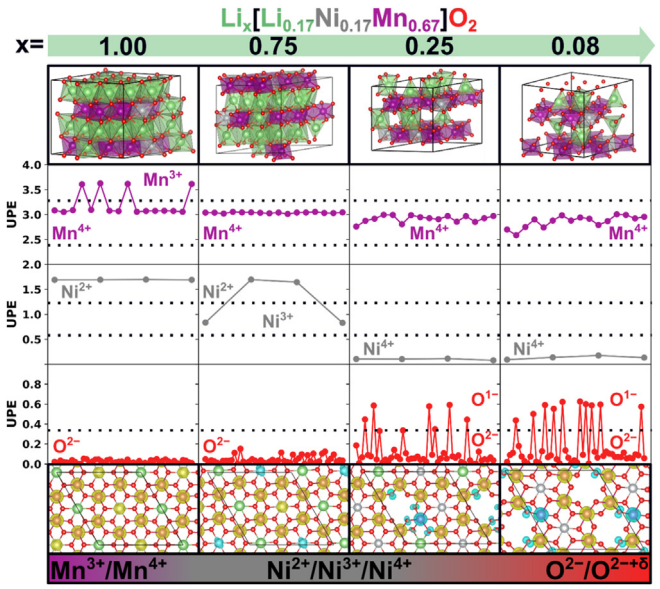

Fig. 5. The lowest-energy geometries obtained from DFT optimizations of MLFF-AIMD images. Number of absolute UPEs on Mn, Ni, and O ions as obtained from the HSE06 electronic structures of the optimized geometries. Formal oxidation states are indicated by dashed lines, whereas oxygen oxidation should be interpreted as partial oxidation rather than full oxidation to O^{1-}. SDD plots from the HSE06 electronic structures. Estimated redox activity of different elements as a function of charge state.

can be determined. The resulting UPEs are plotted for Mn, Ni, and O in the middle part of Fig. 5 at the four considered charge states. Li ions are omitted, as they show zero UPEs throughout all calculations. At x = 1.00 in $Li_x[Li_{0.15}Ni_{0.15}Mn_{0.7}]O_2$, most Mn (12 out of 16) show 3 UPEs, and ~3.7 UPEs are localized on four distinctive Mn. Knowing that Mn ions are coordinated octahedrally by oxygen, ligand-field theory can be applied, splitting the *d*-orbitals into t_{2g} and e_g. Consequently, the 3 UPEs could correspond to a $t_{2g}{}^3e_g{}^0$ electronic configuration that can be assigned to Mn^{4+} ions, whereas 4 UPEs would hint at a $t_{2g}{}^3e_g{}^1$ high-spin configuration and therefore Mn^{3+} ions. The aforementioned Mn ions with 3.7 UPEs are assigned to Mn^{3+}, and the other Mn ions are assumed to be Mn^{4+}. The computed UPE number of ~3.7 for Mn^{3+} does not perfectly match the theoretical value of 4 UPEs, which may be explained by delocalization. Moreover, it should be mentioned that the calculations show highly localized SDDs because a hybrid functional and its large Hartree–Fock mixing parameter were employed, whereas it is unclear how strongly localized the SDDs are in the real system [45]. Therefore, it is more useful to refer to an average Mn charge of 3.75+ for $x = 1.00$. At this lithium concentration and using the same procedure employed for Mn, Ni showed 1.7 UPEs, corresponding to Ni^{2+} ($t_{2g}{}^6e_g{}^2$), and the oxygens had zero UPEs, resulting in O^{2-} ($2p^6$). On delithiation to $x = 0.75$ in $Li_x[Li_{0.15}Ni_{0.15}Mn_{0.7}]O_2$, all the Mn were oxidized to Mn^{4+} (3 UPEs). This observation is in agreement with the Mn redox activity assigned from the experimental *o*-XANES spectra in Fig. 4b, demonstrating Mn^{4+} upon delithiation and a reduction to $Mn^{3.75+}$ for the fully discharged state.

The UPE calculations in Fig. 5 also reveal that two out of four Ni become oxidized to Ni^{3+} ($t_{2g}{}^6e_g{}^1$, 1 UPE theoretical, ~0.8 UPE calculated) at $x = 0.75$, resulting in an average charge of $Ni^{2.5+}$. These findings are also in agreement with the Ni^{2+}/Ni^{4+} redox observed at the beginning of charging in the experiment. Consequently, all of the Ni was further oxidized to Ni^{4+} ($t_{2g}{}^6e_g{}^0$, 0 UPE theoretically, ~0.1 UPE calculated) in the next calculated charge state of $x = 0.25$ in $Li_x[Li_{0.15}Ni_{0.15}Mn_{0.7}]O_2$.

At this state of charge, the UPE on some oxygens starts to deviate from zero, indicating the initial stage of anionic redox. The UPEs are again mainly localized on several specific oxygen ions, with some ions showing as much as 0.6 UPE, which is closer to the UPE value of 1 for an O^{1-} ($2p^5$) than to 0 UPE for an O^{2-} ($2p^6$). However, considering the total fluctuations of UPE on oxygen, and ensuring charge neutrality (Table S6), an average oxidation to $O^{1.875-}$ can be assigned. These findings are again in agreement with the experimental ones, such as the decrease in diffusivity below $x = 0.55$ in $Li_x[Li_{0.15}Ni_{0.15}Mn_{0.7}]O_2$ in Fig. S11a, which was assigned to the initial stage of anionic redox. In the simulated composition representing the highest charging level at $x = 0.08$, only the UPE on oxygen changed significantly compared to that at $x = 0.25$. The slightly increasing fluctuations on Mn might be attributed to delocalization, exchange, disordered coordination environments, or errors. These considerations result in an average oxidation to $O^{1.79-}$ at $x = 0.08$ (refer to Table S6 for estimated charge assignment from UPE), whereas the UPEs are again strongly localized on certain oxygen ions. The strong anionic redox in the highly charged states accords with the experimental findings and the redox activity, which, as observed in the calculations, can be approximated as a function of charge by the colored bar shown in Fig. 5. Interestingly, plotting the SDD (see Fig. 5) reveals that the strongly oxidized oxygens at $x = 0.25$ and $x = 0.08$ are located in direct proximity to TM layer vacancies emerging from the aforementioned migration of Li towards the Li sites. This finding proves the experimental hypothesis that oxygens next to the TM layer vacancies are activated for anionic redox in the LLNM cathode material.

The redox reaction of lattice oxygen in the Li–O–Li configuration leads to the formation of unpaired electrons in the O 2*p* orbital, and Li in the TM layer simultaneously migrates to the Li layer. The ^{7}Li NMR with the pj MATPASS pulse sequence yielded spectra of isotropic shifts without spinning sidebands (Fig. 6a). The rather complicated signals were broader than those of $LiMnO_2$ or Li_2MnO_3 due to the various TM ion configurations. The Li_{Li} and Li_{TM} peaks ranged from 250 to 1200 ppm and from 1300 to 1600 ppm, respectively. The fresh LNNM showed jagged peaks for Li_{Li}, corresponding to a complicated Li site with a mixed three-phase structure. The peak at 844 ppm was assigned to Li_{Li} at tetrahedral sites in the cubic spinel phase domains, which is consistent with the Rietveld refinement results from NPD with the fresh powder (Fig. 1a–S4, S5, S12, S13, Tables S4, S7–S11). It is surprising that in the fully charged state (4.8 V), no Li was detected in the TM layer at the Li_{TM} position, clearly indicating that almost all the Li had migrated out of that layer. Additionally, the significantly lower and broader signal in the Li_{Li} region suggests that a small portion of Li still remained in the Li layer after charging to 4.8 V. This residual Li is attributed to the migration of Li from the TM layer. It appears to distribute across the entire Li_{Li} region, with a peak maximum at 750 ppm. This peak corresponds to a new position of Li in the Li_{Li} tetrahedral site, distinct from the position of Li in the fresh cubic spinel structure at 844 ppm and exhibiting greater intensity than the octahedral site within the Li layer. In the fully discharged state (2 V), Li_2CO_3-like cathode–electrolyte interphase (CEI) species were evidenced by the sharp peak near 0 ppm, which accorded with the surface observation measured using the total electron yield (TEY) mode for the O K-edge spectra (Fig. S12). In comparison to the fresh state, the Li_{TM} accounted for ~13.2%, compared to 86.2% for Li_{Li}. These results indicate that a portion of the Li was not recovered to the fresh state, and that it is favorable for Li to be located in the Li layers or as part of the CEI layer. Additionally, the peaks in the discharged state were broader than in the initial state, which can be attributed to the rearrangement of TMs caused by Li migration and the additional Li insertion to $x = 0.95$ in $Li_x[Li_{0.15}Ni_{0.15}Mn_{0.7}]O_2$.

As observed in the ^{7}Li NMR spectra in Fig. 6a, migration of the excess lithium in the TM sites towards the lithium sites occurred on charge. According to the MLFF-AIMD simulations (Fig. S8 and Table S6), no Li migration occurred at $x = 1.00$ and $x = 0.75$ in $Li_x[Li_{0.15}Ni_{0.15}Mn_{0.7}]O_2$, whereas at $x = 0.25$, 75% (3 out of 4 ions) of the TM layer lithium migrated, and at $x = 0.08$, 100% (4 out of 4 ions) migrated. Moreover, simulations reveal that the Li ions in the Li layers also become more disordered; here, "disordered" does not indicate decomposition or instability but refers to minor displacements from the positions in the perfect crystal structure. This trend was observed because the probability of having Li in a tetrahedral environment increases for higher charged structures, as indicated in the histograms in Fig. 6b. At $x = 1.00$, most of the lithium is almost always in an octahedral environment (6 oxygens), whereas the probability of other coordination environments becomes more equal on delithiation, and at $x = 0.08$, a tetrahedral (4 oxygens) environment is highly probable. Notably, the abovementioned changes in lattice parameters can affect how many oxygens are found in a sphere of fixed radius. In addition, the amount of lithium environments the probability is calculated from varies with *x*, as fewer lithium coordinations can be considered per structure at lower *x* values. Nevertheless, the trend indicates that the structures become more disordered at highly charged states and that lithium likely starts to occupy tetrahedral sites in the structure as well.

The Li migration and the resulting structural disorder were further elucidated through NPD data, ICP analysis, and STEM observations (Figs. 6c–g, Tables S7–S9). The STEM and SAED images of the delithiated electrode indicated the presence of the original O2 phase (Fig. 6f), although Li ions had migrated out of the TM layer (Figs. 6a and c, Table S6). ICP-AES analysis of the charged electrode verified that 0.05 mol Li remained in the structure (Table S9), which is consistent with the NPD data. This finding indicates that the migration of Li creates vacancies (V_{Li}) in the TM layer, and this structural disorder is most likely initiated by Li migration from the TM layer to the Li layers. This phenomenon led to disorder of the Li/V_{Li}/Mn/Ni in the TM layer, resulting in declination of the in-plane ordering. As a result, the signals of the TM in the charged LLNM electrode material were significantly blurred and partially lost their ordering in some parts of the observed image (Fig. 6f), compared to the fresh state (Fig. 6e). This process resulted in unpaired electrons in the presence of the Li–O–Li configuration, triggering the oxidation of the lattice oxygen and simultaneously reducing the O–O distance. Furthermore, the interlayer distance was shortened by the highly covalent character of the TM layer ($d \approx 4.68$ Å). After discharge, the layered structure was retained upon lithiation to $x \approx 0.95$ in $Li_x[Li_{0.15}Ni_{0.15}Mn_{0.7}]O_2$ (Fig. 6d), and the in-plane ordering was not fully restored in the NPD and SAED patterns (Fig. 6g). The present O2-type $Li_{0.75}[Li_{0.15}Ni_{0.15}Mn_{0.7}]O_2$, Li-excess LLNM material has the Li–O–Li configuration. The condition for the formation of unpaired electrons in the oxygen 2*p* orbital occurs as Li in the TM layer simultaneously migrates to the Li layer during the oxidation of lattice oxygen. This migration is facilitated by the comparatively low ionization energy of Li^+ (520.2 kJ mol^{-1}) relative to that of transition metal elements such as Ni^{2+} (2226.3 kJ mol^{-1}), Ni^{3+} (5474.7 kJ mol^{-1}), Ni^{4+} (10,414.7 kJ mol^{-1}), and Mn^{4+} (10,414.7 kJ mol^{-1}) [46].

Based on the results of ND diffraction, STEM images, and thermodynamic simulations, Li migration was evident from the octahedrally coordinated TM layer to the Li layers. However, the migration of TM elements from the TM layer to the Li layers during de/lithiation does not seem to have occurred in our O2-type LLMO cathode material, as would be possible if the Mn ion were in a tetrahedral environment with much higher oxidation states, such as Mn^{5+}, Mn^{6+}, or Mn^{7+} at higher voltages [47].

Since the in-plane ordering was not fully recovered, the cycled electrodes were compared with the fresh O2-LLNM material (Fig. S15). The superstructure observed at approximately 21° (2θ) was no longer visible after 50 cycles. This suggests that the gradual capacity fading during the initial 50 cycles observed in Fig. 2d is likely associated with the disordering of the TM layer, where Li and Ni elements coexist with Mn. The XRD data obtained after 500 cycles shows no significant changes in the XRD pattern, except a change in the relative intensity of the Bragg peaks compared to the pattern after 50 cycles. Nonetheless, the O2 structural

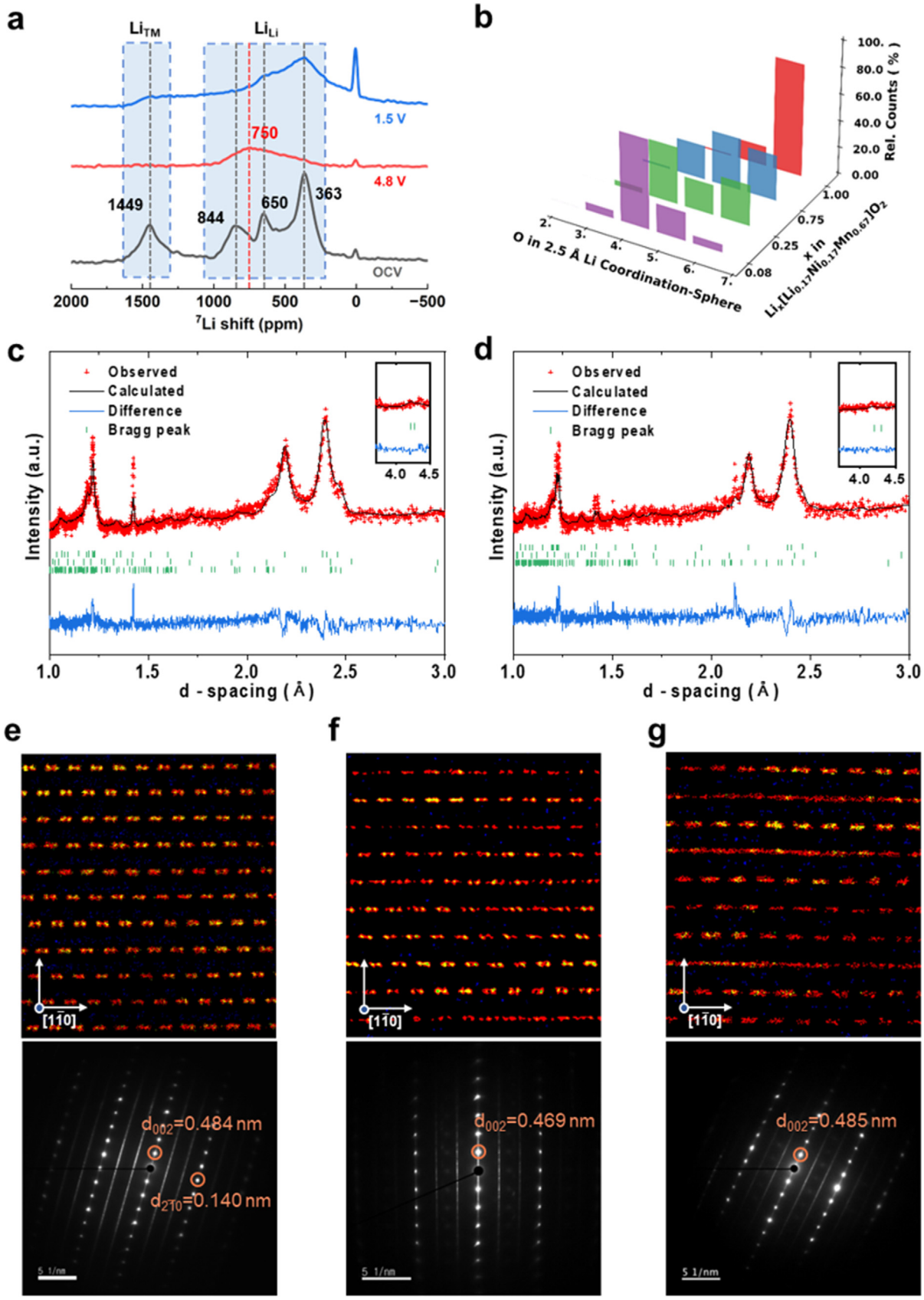

Fig. 6. Investigation of the local Li environment. (a) ^{7}Li NMR spectra for pristine, charged, and discharged LLNM. (b) Histograms of oxygen counts within a 2.5 Å coordination sphere around Li ions at different charge states from the MLFF-AIMD simulations. (c) NPD pattern of charged LLNM. (d) NPD pattern of discharged LLNM. (e, f, g) STEM images and SAED patterns for fresh, charged, and discharged LLNM.

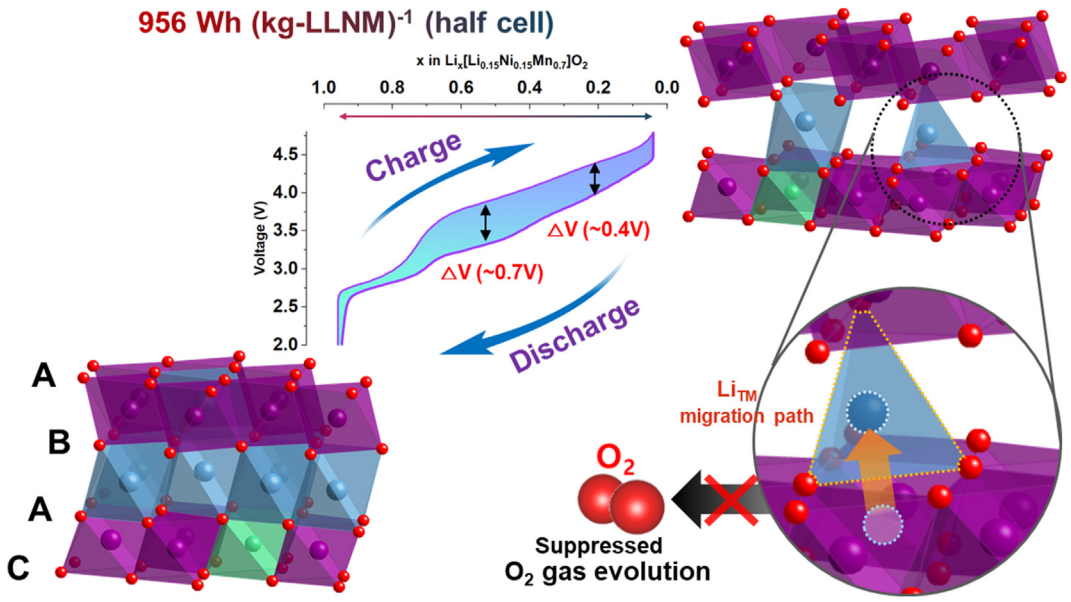

Fig. 7. Illustration of LLNM characteristics.

framework remained even after 500 cycles. Recent publications have not mentioned the theoretical capacity of the O2-type cathode material [23, 27]. In our study, we define the theoretical capacity of O2-LLNM as 313 mAh g^{-1}: note that $Li_{1.00}[Li_{0.25}Co_{0.25}Mn_{0.50}]O_2$ [27] exhibited a capacity of over 400 mAh g^{-1}, which exceeds the theoretical limit, although the related charge storage mechanism was not clarified. Our O2–$Li_{0.75}[Li_{0.15}Ni_{0.15}Mn_{0.7}]O_2$ demonstrates reasonable long-term cycling performance, with better voltage retention and capacity retention during cycling. Earlier O2-type materials, while showing high initial capacities, tend to experience rapid voltage fade [25,27]. The full cell delivered an initial discharge capacity of 272 g^{-1} at 0.1C (Fig. 2d), and the resulting retention was ~70% after 500 cycles at 0.5C. In comparison with the performance of electrodes reported in other studies [22,25, 27–33] (Table S12), the present O2–$Li_{0.75}[Li_{0.15}Ni_{0.15}Mn_{0.7}]O_2$ cathode material has superior structural stability and cyclability.

This Mn-based, Co-free, reduced-nickel LLNM compound holds significant potential for next-generation LIBs, addressing key challenges such as environmental sustainability, cost reduction, and high energy density. Its specific capacity in excess of 280 mAh g^{-1}, high energy density of ~956 Wh kg^{-1}, thermal stability, and stable cycling performance demonstrate its viability for practical applications (Fig. 7 and Fig. S16). The migration of Li ions from the TM layer to the Li layers triggers the oxygen redox reaction in the presence of the Li–O–Li configuration. An advantage of this process is that it suppresses the structural disintegration caused by O_2 evolution and phase transition. Capacity retention and long-term cycling stability could be further improved by developing strategies to enhance the structural integrity of the TM layers or designing new structural motifs that better accommodate lithium migration.

In summary, our LLNM cathode material offers a compelling solution for safety-enhanced high-capacity LIBs. By addressing the challenges related to electrolyte and interface stability at high voltage, this material could play a pivotal role in the development of next-generation energy storage technologies.

4. Conclusions

This study presents O2-type Li-excess $Li_{0.75}[Li_{0.15}Ni_{0.15}Mn_{0.7}]O_2$ (LLNM) as a highly promising cathode material for next-generation LIBs, offering significant advances in terms of capacity, retention, and structural stability. We highlight the role of Li migration out of the TM layer and its contribution to the activation of reversible lattice oxygen redox in the presence of Li–O–Li configurations. Electrochemical tests demonstrated exceptional capacity retention, thermal stability, and cycling durability, with LLNM achieving 284 mAh g^{-1} and 956 Wh kg^{-1} over 200 cycles and maintaining 70% capacity retention after 500 cycles in full-cell configurations. Unlike previous reports, which often emphasize high capacities without addressing reaction and degradation mechanisms, our study provides a pathway for balancing high energy density and long-term cycling stability. Through comprehensive experimental and computational analyses, we found that the distinct oxygen lattice of the O2 stacking in the LLNM effectively suppresses phase transition and oxygen evolution from the structure during de/lithiation. The Li-excess composition in the TM layer enabled substantial charge storage, facilitated by both oxygen redox and TM (Ni, Mn) redox reactions. We further elucidate that Li migration from the TM to the Li layers facilitates reversible charge compensation, effectively suppressing structural degradation while maintaining an O2 framework, even after prolonged cycling. These findings offer a mechanistic understanding of the synergistic contributions of the cationic and anionic redox reactions, which have not been sufficiently explored in earlier studies. Based on theoretical and experimental investigation, this research offers innovative insights into the development of Co-free, reduced-nickel cathode materials, thereby addressing key challenges in the design of sustainable and high-performance cathode materials for LIBs.

CRediT authorship contribution statement

Jun Ho Yu: Writing – review & editing, Writing – original draft, Validation, Supervision, Resources, Project administration, Methodology, Investigation, Formal analysis, Data curation, Conceptualization. **Konstantin Köster:** Visualization, Validation, Supervision, Software, Resources, Methodology, Investigation, Formal analysis, Data curation, Conceptualization. **Natalia Voronina:** Funding acquisition, Formal analysis, Data curation. **Sungkyu Kim:** Visualization, Validation, Formal analysis, Data curation. **Hyeon-Ji Shin:** Formal analysis, Data curation. **Kyung Sun Kim:** Formal analysis, Data curation. **Kyuwook Ihm:** Formal analysis, Data curation. **Hyungsub Kim:** Formal analysis, Data curation. **Hun-Gi Jung:** Formal analysis, Data curation. **Koji Yazawa:** Formal analysis, Data curation. **Olivier Guillon:** Methodology, Investigation, Formal analysis, Data curation. **Pierluigi Gargiani:** Formal analysis, Data curation. **Laura Simonelli:** Writing – review & editing,

Visualization, Validation, Methodology, Investigation, Formal analysis, Data curation, Conceptualization. **Payam Kaghazchi:** Writing – review & editing, Writing – original draft, Validation, Supervision, Methodology, Investigation, Funding acquisition, Formal analysis, Data curation, Conceptualization. **Seung-Taek Myung:** Writing – review & editing, Writing – original draft, Visualization, Validation, Supervision, Software, Resources, Project administration, Methodology, Investigation, Funding acquisition, Formal analysis, Data curation, Conceptualization.

Declaration of competing interest

The authors declare no competing financial interests.

Acknowledgments

This research was supported by Basic Science Research Program through the National Research Foundation of Korea (NRF) funded by the Ministry of Education, Science and Technology (NRF-2022R1F1A1063351 and RS-2024-00446825). Experiments at PLS-II were supported in part by MSIT and POSTECH. K. Köster and P. Kaghazchi gratefully acknowledge the computing time granted through JARA-HPC on the supercomputer JURECA [48] at Forschungszentrum Jülich under Grant No. jiek12 and funding from the "Deutsche Forschungsgemeinschaft" (DFG, German Research Foundation) under Project No. 501562980.

Appendix A. Supplementary data

Supplementary data to this article can be found online at https://doi.org/10.1016/j.esci.2025.100376.

References

[1] J.M. Paulsen, J.R. Mueller-Neuhaus, J.R. Dahn, Layered $LiCoO_2$ with a different oxygen stacking (O2 Structure) as a cathode material for rechargeable lithium batteries, J. Electrochem. Soc. 147 (2000) 508.
[2] M. Bianchini, M. Roca-Ayats, P. Hartmann, T. Brezesinski, J. Janek, There and back again-the journey of $LiNiO_2$ as a cathode active material, Angew. Chem. Int. Ed. 58 (2019) 10434–10458.
[3] J.M. Paulsen, C.L. Thomas, J.R. Dahn, Layered Li-Mn-Oxide with the O2 structure: a cathode material for Li-ion cells which does not convert to spinel, J. Electrochem. Soc. 146 (1999) 3560.
[4] Y. Lyu, X. Wu, K. Wang, Z. Feng, T. Cheng, Y. Liu, M. Wang, R. Chen, L. Xu, J. Zhou, Y. Lu, B. Guo, An overview on the advances of $LiCoO_2$ cathodes for lithium-ion batteries, Adv. Energy Mater. 11 (2021) 2000982.
[5] N.S. Luu, P.E. Meza, A.M. Tayamen, O. Kahvecioglu, S.V. Rangnekar, J. Hui, J.R. Downing, M.C. Hersam, Enabling ambient stability of $LiNiO_2$ lithium-ion battery cathode materials via graphene-cellulose composite coatings, Chem. Mater. 35 (2023) 5150–5159.
[6] B. Dong, A.D. Poletayev, J.P. Cottom, J. Castells-Gil, B.F. Spencer, C. Li, P. Zhu, Y. Chen, J.M. Price, L.L. Driscoll, P.K. Allan, E. Kendrick, M.S. Islam, P.R. Slater, Effects of sulfate modification of stoichiometric and lithium-rich $LiNiO_2$ cathode materials, J. Mater. Chem. A 12 (2024) 11390–11402.
[7] T. Chen, J. Yang, L. Barroso-Luque, G. Ceder, Removing the two-phase transition in spinel $LiMn_2O_4$ through cation disorder, ACS Energy Lett. 8 (2023) 314–319.
[8] J.H. Kim, S.T. Myung, C.S. Yoon, S.G. Kang, Y.K. Sun, Comparative study of $LiNi_{0.5}Mn_{1.5}O_{4-\delta}$ and $LiNi_{0.5}Mn_{1.5}O_4$ cathodes having two crystallographic structures: Fd-3m and $P4_332$, Chem. Mater. 16 (2004) 906–914.
[9] X. Dong, Y. Xu, S. Yan, S. Mao, L. Xiong, X. Sun, Towards low-cost, high energy density Li_2MnO_3 cathode materials, J. Mater. Chem. A 3 (2015) 670–679.
[10] J. Song, H. Wang, Y. Zuo, K. Zhang, T. Yang, Y. Yang, C. Gao, T. Chen, G. Feng, Z. Jiang, W. Xiao, T. Luo, D. Xia, Building better full manganese-based cathode materials for next-generation lithium-ion batteries, Electrochem. Energy Rev. 6 (2023).
[11] T. Liu, J. Liu, L. Li, L. Yu, J. Diao, T. Zhou, S. Li, A. Dai, W. Zhao, S. Xu, Y. Ren, L. Wang, T. Wu, R. Qi, Y. Xiao, J. Zheng, W. Cha, R. Harder, I. Robinson, J. Wen, J. Lu, F. Pan, K. Amine, Origin of structural degradation in Li-rich layered oxide cathode, Nature 606 (2022) 305–312.
[12] K. Kawai, X.M. Shi, N. Takenaka, J. Jang, B.M. de Boisse, A. Tsuchimoto, D. Asakura, J. Kikkawa, M. Nakayama, M. Okubo, A. Yamada, Kinetic square scheme in oxygen-redox battery electrodes, Energy Environ. Sci. 15 (2022) 2591–2600.
[13] J.M. Paulsen, D. Larcher, J.R. Dahn, O2 structure $Li_{2/3}[Ni_{1/3}Mn_{2/3}]O_2$: a new layered cathode material for rechargeable lithium batteries III. Ion exchange, J. Electrochem. Soc. 147 (2000) 2862.
[14] N. Yabuuchi, R. Hara, M. Kajiyama, K. Kubota, T. Ishigaki, A. Hoshikawa, S. Komaba, New O2/P2-type Li-excess layered manganese oxides as promising multi-functional electrode materials for rechargeable Li/Na batteries, Adv. Energy. Mater. 4 (2014) 1301453.
[15] X. Cao, Y. Qiao, M. Jia, P. He, H. Zhou, Ion-exchange: a promising strategy to design Li-rich and Li-excess layered cathode materials for Li-ion batteries, Adv. Energy Mater. 12 (2022) 2003972.
[16] J. Hong, D.H. Seo, S.W. Kim, H. Gwon, S.T. Oh, K. Kang, Structural evolution of layered $Li_{1.2}Ni_{0.2}Mn_{0.6}O_2$ upon electrochemical cycling in a Li rechargeable battery, J. Mater. Chem. 20 (2010) 10179–10186.
[17] P.M. Csernica, K. McColl, G.M. Busse, K. Lim, D.F. Rivera, D.A. Shapiro, M.S. Islam, W.C. Chueh, Substantial oxygen loss and chemical expansion in lithium-rich layered oxides at moderate delithiation, Nat. Mater. 24 (2025) 92–100.
[18] K. McColl, S.W. Coles, P. Zarabadi-Poor, B.J. Morgan, M.S. Islam, Phase segregation and nanoconfined fluid O_2 in a lithium-rich oxide cathode, Nat. Mater. 23 (2024) 826–833.
[19] L.L. Zhang, J.J. Chen, S. Cheng, H.F. Xiang, Enhanced electrochemical performances of $Li_{1.2}Ni_{0.2}Mn_{0.6}O_2$ cathode materials by coating $LiAlO_2$ for lithium-ion batteries, Ceram. Int. 42 (2016) 1870–1878.
[20] Q. Li, D. Ning, D. Wong, K. An, Y. Tang, D. Zhou, G. Schuck, Z. Chen, N. Zhang, X. Liu, Improving the oxygen redox reversibility of Li-rich battery cathode materials via coulombic repulsive interactions strategy, Nat. Commun. 13 (2022) 1123.
[21] Q. Jiang, X. Li, Y. Hao, J. Zuo, R. Duan, J. Li, G. Cao, J. Wang, J. Wang, M. Li, X. Yang, M. Li, W. Li, Y. Xi, J. Zhang, W. Xiao, Oxygen-vacancy-assisted dual functional surface coatings suppressing irreversible phase transition of Li-rich layered oxide cathodes, Adv. Funct. Mater. (2024) 2400670.
[22] X. Cao, H. Li, Y. Qiao, M. Jia, P. He, J. Cabana, H. Zhou, Achieving stable anionic redox chemistry in Li-excess O2-type layered oxide cathode via chemical ion-exchange strategy, Energy Stor. Mater. 38 (2021) 1–8.
[23] D. Eum, B. Kim, S.J. Kim, H. Park, J. Wu, S.P. Cho, G. Yoon, M.H. Lee, S.K. Jung, W. Yang, W.M. Seong, K. Ku, O. Tamwattana, S.K. Park, I. Hwang, K. Kang, Voltage decay and redox asymmetry mitigation by reversible cation migration in lithium-rich layered oxide electrodes, Nat. Mater. 19 (2020) 419–427.
[24] X. Cao, H. Li, Y. Qiao, M. Jia, H. Kitaura, J. Zhang, P. He, J. Cabana, H. Zhou, Structure design enables stable anionic and cationic redox chemistry in a T2-type Li-excess layered oxide cathode, Sci. Bull. 67 (2022) 381–388.
[25] H. Shang, Y. Zuo, F. Shen, J. Song, F. Ning, K. Zhang, L. He, D. Xia, O2-type $Li_{0.78}[Li_{0.24}Mn_{0.76}]O_2$ nanowires for high-performance lithium-ion battery cathode, Nano Lett 20 (2020) 5779–5785.
[26] Y. Chen, Y. Liu, J. Zhang, H. Zhu, Y. Ren, W. Wang, Q. Zhang, Y. Zhang, Q. Yuan, G.X. Chen, L.C. Gallington, K. Li, X. Liu, J. Wu, Q. Liu, Y. Chen, Constructing O2/O3 homogeneous hybrid stabilizes Li-rich layered cathodes, Energy Stor. Mater. 51 (2022) 756–763.
[27] Y. Zuo, B. Li, N. Jiang, W. Chu, H. Zhang, R. Zou, D. Xia, A High-Capacity O2-type Li-rich cathode material with a single-layer Li_2MnO_3 superstructure, Adv. Mater. 30 (2018) 1707255.
[28] D. Eum, S.O. Park, H.Y. Jang, Y. Jeon, J.H. Song, S. Han, K. Kim, K. Kang, Electrochemomechanical failure in layered oxide cathodes caused by rotational stacking faults, Nat. Mater. 23 (2024) 1093–1099.
[29] H. Liu, X. Wu, X. Lou, W. Tong, J. Li, B. Hu, C. Li, The influence of Li deficiency: an overlooked factor that determines the anion redox reversibility of Mn-based layered oxide cathodes, Energy Stor. Mater. 63 (2023) 103058.
[30] D. Eum, H.Y. Jang, B. Kim, J. Chung, D. Kim, S.P. Cho, S.H. Song, S. Kang, S. Yu, S.O. Park, J.H. Song, H. Kim, O. Tamwattana, D.H. Kim, J. Lim, K. Kang, Effects of cation superstructure ordering on oxygen redox stability in O2-type lithium-rich layered oxides, Energy Environ. Sci. 16 (2023) 673–686.
[31] X. Yang, K. Wang, J. Zhang, H. Li, H. Liu, T. Zhao, X. Zhai, Q. Wang, C. Fan, M. Etter, S. Indris, W. Hua, X. Ouyang, Modulating local oxygen coordination to achieve highly reversible anionic redox and negligible voltage decay in O2-type layered cathodes for Li-ion batteries, Adv. Energy Mater. (2024) 2404276.
[32] C. Cui, X. Fan, X. Zhou, J. Chen, Q. Wang, L. Ma, C. Yang, E. Hu, X.Q. Yang, C. Wang, Structure and interface design enable stable Li-rich cathode, J. Am. Chem. Soc. 142 (2020) 8918–8927.
[33] Z. Yang, J. Zhong, J. Feng, J. Li, F. Kang, Highly reversible anion redox of manganese-based cathode material realized by electrochemical ion exchange for lithium-ion batteries, Adv. Funct. Mater. 31 (2021) 2103594.
[34] B.M. de Boisse, J. Jang, M. Okubo, A. Yamada, Cobalt-free O2-type lithium-rich layered oxides, J. Electrochem. Soc. 165 (2018) A3630–A3633.
[35] R.A. House, U. Maitra, M.A. Pérez-Osorio, J.G. Lozano, L. Jin, J.W. Somerville, L.C. Duda, A. Nag, A. Walters, K.J. Zhou, M.R. Roberts, P.G. Bruce, Superstructure control of first-cycle voltage hysteresis in oxygen-redox cathodes, Nature 577 (2020) 502–508.
[36] S. Komaba, K. Yoshii, A. Ogata, I. Nakai, Structural and electrochemical behaviors of metastable $Li_{2/3}[Ni_{1/3}Mn_{2/3}]O_2$ modified by metal element substitution, Electrochim. Acta 54 (2009) 2353–2359.
[37] X. Wang, Q. Zhang, C. Zhao, H. Li, B. Zhang, G. Zeng, Y. Tang, Z. Huang, I. Hwang, H. Zhang, S. Zhou, Y. Qiu, Y. Xiao, J. Cabana, C.J. Sun, K. Amine, Y. Sun, Q. Wang, G.L. Xu, L. Gu, Y. Qiao, S.G. Sun, Achieving a high-performance sodium-ion pouch cell by regulating intergrowth structures in a layered oxide cathode with anionic redox, Nat. Energy 9 (2024) 184–196.
[38] Y. Tang, Q. Zhang, W. Zuo, S. Zhou, G. Zeng, B. Zhang, H. Zhang, Z. Huang, L. Zheng, J. Xu, W. Yin, Y. Qiu, Y. Xiao, Q. Zhang, T. Zhao, H.G. Liao, I. Hwang, C.J. Sun, K. Amine, Q. Wang, Y. Sun, G.L. Xu, L. Gu, Y. Qiao, S.G. Sun, Sustainable layered cathode with suppressed phase transition for long-life sodium-ion batteries, Nat. Sustain. 7 (2024) 348–359.
[39] V. Saïbi, L. Castro, I. Sugiyama, S. Belin, C. Delmas, M. Guignard, Stacking faults in an O2-type cobalt-free lithium-rich layered oxide: mechanisms of the ion exchange

reaction and lithium electrochemical (de)intercalation, Chem. Mater. 35 (2023) 8540–8550.
[40] V.F. Sears, Special feature neutron scattering lengths and cross sections, Neutron News 3 (1992) 26.
[41] C. Zhao, C. Li, H. Liu, Q. Qiu, F. Geng, M. Shen, W. Tong, J. Li, B. Hu, Coexistence of $(O_2)^{n-}$ and trapped molecular O_2 as the oxidized species in P2-type sodium 3d layered oxide and stable interface enabled by highly fluorinated electrolyte, J. Am. Chem. Soc. 143 (2021) 18652–18664.
[42] M. Sathiya, J.B. Leriche, E. Salager, D. Gourier, J.M. Tarascon, H. Vezin, Electron paramagnetic resonance imaging for real-time monitoring of Li-ion batteries, Nat. Commun. 6 (2015) 6276.
[43] C. Li, C. Zhao, B. Hu, W. Tong, M. Shen, B. Hu, Unraveling the critical role of Ti substitution in P2-$Na_xLi_yMn_{1-y}O_2$ cathodes for highly reversible oxygen redox chemistry, Chem. Mater. 32 (2020) 1054–1063.
[44] M. Tang, A. Dalzini, X. Li, X. Feng, P.H. Chien, L. Song, Y.Y. Hu, Operando EPR for simultaneous monitoring of anionic and cationic redox processes in Li-rich metal oxide cathodes, J. Phys. Chem. Lett. 8 (2017) 4009–4016.
[45] K. Köster, P. Kaghazchi, Hybrid functionals with nonempirical Hartree-Fock parameters for electronic structure calculation of layered oxides, Phys. Rev. B 109 (2024) 155134.
[46] Ionization energies of the elements. https://periodictable.com/Properties/A/IonizationEnergies.an.html.
[47] M.D. Radin, J. Vinckeviciute, R. Seshadri, A. Van der Ven, Manganese oxidation as the origin of the anomalous capacity of Mn-containing Li-excess cathode materials, Nat. Energy 4 (2019) 639–646.
[48] Jülich Supercomputing Centre, JURECA: data centric and booster modules implementing the modular supercomputing architecture at Jülich supercomputing centre, J. large-scale Res. Facil. 7 (2021) A182.